JOURNAL OF AIRCRAFT
Vol. 44, No. 1, January–February 2007

Wake Vorticity Measurements for Low Aspect Ratio Wings at Low Reynolds Number

Sergey M. Kaplan* and Aaron Altman†
University of Dayton, Dayton, Ohio 45469-0238
and
Michael Ol‡
Air Force Research Laboratory, Wright–Patterson Air Force Base, Ohio 45433-7542

DOI: 10.2514/1.23096

Trailing vortex structure of low aspect ratio wings was studied in a water tunnel at Reynolds numbers of 8000 and 24,000 using dye injection and digital particle image velocimetry in cross-flow planes in the near wake, for rectangular, semi-elliptical, and delta-wing planforms. The velocity data were used to calculate lift via circulation and effective span, and the results were compared with force balance measurements and classical inviscid theory. The objectives of the study were to assess how low-Reynolds number effects might affect the measurement of lift coefficient from tip-vortex circulation, how well the measurements fit the various theoretical models of lift curve slope for low aspect ratio wings, and the extent to which planform shape affects lift coefficient while aspect ratio and planform area are kept constant. All models were thin flat plates with square edges. For the conditions studied, apparent viscous effects on vorticity integrations in the wake were small, resulting in good agreement between lift coefficient values inferred from the measurements, the force balance data, and the classical inviscid formulas. Whereas the three wings exhibited distinctly different wake structures, lift curve slopes were similar.

Nomenclature

AR	=	wing aspect ratio
b	=	wing span
b'	=	effective span
C_L	=	wing lift coefficient
$\bar{c}$	=	wing mean aerodynamic chord
K_P	=	attached-flow lifting surface theory parameter
K_V	=	vortex-lift parameter
L	=	total lift
r/b	=	normalized radius of vortex
S	=	wing planform area
U_x	=	magnitude of in-plane velocity in cross-flow planes
U_∞	=	freestream velocity
V	=	velocity in yz plane
X/C	=	normalized distance downstream of the trailing edge
Y/b	=	normalized distance in the spanwise direction
Z/C	=	normalized distance perpendicular to freestream direction
α	=	geometric angle of attack
Γ	=	circulation
ρ_∞	=	freestream density
$\varphi_{1/2c}$	=	midchord line sweep angle
ω_x	=	vorticity in yz (cross-flow) plane

Introduction

MICRO air vehicles (MAVs) tend to have low aspect ratio wings [1], thus motivating a revisit of classical slender-wing results. Whereas typical fixed rigid-wing MAVs of the present generation operate at $Re \sim 100,000$ [2], two applications call for extension to lower Reynolds numbers: flexible-wing MAVs [3] and flapping-wing configurations [4]. In either case, it is useful to commence with a parameter study of the rigid wing of small aspect ratio in nominally steady flow. This approach is amenable to relatively traditional experimental methods, as a baseline case for the more complex studies of flexibility and unsteadiness. Recent work on laminar separations for 2-D airfoils at Reynolds numbers less than 100,000, both experimental [5] and computational [6], has continued a rich tradition of research on the role of flow separation, transition in shear layers bounding airfoil laminar separation bubbles, and unsteady reattachment. This work has elucidated the resulting decline in lift to drag ratio and rise of unsteadiness with decreasing Reynolds number. However, in going from 2-D airfoils to the more applied problem of low aspect ratio wings for MAVs, these effects seem to be rather attenuated [7]. It can be further stipulated that thin plates with sharp leading edges more or less fix the transition point. Gursul et al. [8] discuss comparative Reynolds number insensitivity for sharp-edged low aspect ratio wings, at least for Reynolds numbers above approximately 20,000. Spedding et al. [9] report that at $Re = 12,000$ and AR $= 6$, flat-plate airfoils produced higher lift to drag ratio and more gentle stall than some low-Reynolds number optimized airfoil sections. Use of such thin flat-plate "airfoils" allows for the isolation of planform effects, rather than airfoil sectional effects.

In looking at numerous planform shapes in an aspect ratio range from 0.5 to 2, at Reynolds numbers from 70,000 to 140,000, Torres and Mueller [10] showed increasing nonlinearity in the lift curve slope and an increase in stall angle of attack as the aspect ratio decreased. Besides 2-D low-Reynolds number effects identified earlier by Mueller [11], such nonlinearity could be due to loss of leading-edge suction and the turning of the resulting force vector into the flow-normal direction [12]. The latter should not be a Reynolds number dependent effect.

Laitone [13] studied rectangular planform wings at Reynolds numbers near 20,000, taking force balance lift and drag measurements for flat and cambered plates in a wind tunnel. For this Reynolds number, an aspect ratio of 6 was used for all the models, whereas aspect ratios of 2.18, 4, and 8 were used only for rectangular flat plates. The results for the rectangular flat-plate wing

Presented as Paper 0246 at the Aerospace Sciences Conference, Reno, NV, 9–12 January 2006; received 9 February 2006; revision received 23 August 2006; accepted for publication 28 August 2006.

*Graduate Student, Aerospace Engineering Department.
†Assistant Professor, Mechanical and Aerospace Engineering Department, 300 College Park Drive. Senior Member AIAA.
‡Aerospace Engineer, Air Vehicles Directorate, 2310 8th Street, Building 45. Senior Member AIAA.

with an aspect ratio of 2.18 will be used to validate results in the present study.

Further insight into lift behavior at low-Reynolds number may be uncovered by studying the wake. Lowson [14] considered the vortex structure behind a 70-deg delta wing with a chord of 44.1 cm and thickness of 1.2 cm, at Reynolds numbers between 3000 and 30,000. Lowson suggests that in flows with Reynolds numbers below 6600, viscous dissipation forces dominate to such an extent that the high-Reynolds number theories for predicting vortex roll-up behavior and vortex strength breakdown, but that low-Reynolds number experiments can in some instances be used to predict the entire vortex sheet behavior to better understand full-scale model aerodynamic characteristics. Finally, Lowson argues that although there is some disagreement in the vortex roll-up behavior between theoretical high-Reynolds number predictions and low-Reynolds number experiments, the velocity distribution and vortex strength in the wake behind a delta wing at low Reynolds numbers are still consistent with the theoretical predictions for high-Reynolds number flows.

Cosyn and Vierendeels [15] conducted fully turbulent computations on rectangular wings at $Re = 100,000$, finding close agreement with lift predicted by lifting surface theory with Polhamus's leading-edge suction analogy [12]. Zuhal and Gharib [16] studied tip vortices for a NACA 0012 AR ~ 4.6 wing in a wind tunnel at Reynolds numbers close to 9000, with stereoscopic particle image velocimetry (PIV). The authors suggest that the unsteady motion of the wing-tip vortex is a result of an interaction between the main vortex and branching vortices, the strength of the latter conceivably exhibiting a Reynolds number dependency.

The present work begins to consider a parameter study of Reynolds number and angle of attack on lift behavior and on structure of vorticity in the wake for a range of planforms, while keeping aspect ratio and planform area constant. The comparative ease of performing whole-field velocity measurements in the wake rather than in regions including boundary layers, invites a comparison of velocity field measurement, and the relation of lift coefficient for wings of various planform inferred from wake circulation, to that of the classical inviscid theories. Intuitively, if this comparison were favorable, then at least for purposes of lift production the main viscous effects such as vortex shedding from the wing's suction-side would be comparatively unimportant, lending further credence to the assertion that low aspect ratio 3-D effects and sharp-edge effects attenuate the low-Reynolds number performance decline observed for 2-D airfoils. Consideration of aerodynamic loads is limited to lift: or, in the case of direct force measurements, to normal force. As the motivation is more concerned with cruise performance of MAVs, than with maneuvering (where, in any case, steady boundary conditions are of rather tenuous applicability), the focus is on relatively low angles of attack.

Theory

For a slender wing in general, the approximation in Eq. (1) given by Thwaites [17] can be used:

$$C_L = \frac{1}{2}\pi \mathrm{AR}\alpha \tag{1}$$

The approximation can be improved as seen in Eq. (2) to account for the sweep (for the delta wing of AR $= 2$, the leading-edge sweep angle was 63.43 deg and the midchord sweep angle was 45 deg); also from Thwaites [17]:

$$C_L = \frac{1}{2}\pi \mathrm{AR}\alpha\left[\frac{4}{2 + \mathrm{AR}\tan(\varphi_{1/2c})}\right] \tag{2}$$

If an elliptic lift distribution for the semi-elliptical model can be assumed, the lifting-line result (from, e.g., Anderson [18]) is shown in Eq. (3):

$$C_L = \alpha\left[\frac{2\pi}{1 + 2/\mathrm{AR}}\right] \tag{3}$$

Lamar [19], in his discussion of the leading-edge suction analogy extended to low aspect ratio wings of generalized planform, gives an expression for lift coefficient based on lifting-surface theory with a correction for the turning into the normal direction of leading-edge and side-edge suction:

$$C_L = K_P \sin(\alpha)\cos^2(\alpha) + K_V \sin^2(\alpha)\cos(\alpha) \tag{4}$$

K_P, accounting for attached flow, is approximately 2.5 at AR $= 2$, whereas K_V, accounting for the vortical contribution is very close to π [19]. At an aspect ratio of 2, possibly Eq. (1) and especially Eq. (3) are outside of their likely range of applicability, but conveniently, both collapse to $C_L = \pi\alpha$. Also, at AR $= 2$, K_P and K_V are each approximately independent of planform shape.

Experiments

In an attempt to separate airfoil sectional behavior and wing planform behavior, this study focused on thin, blunt-edged flat plates. Tip vortex trajectory and wake structure are qualitatively assessed by flow visualization with dye injection (food coloring mixed in various concentrations with water). Digital particle image velocimetry (DPIV) is used to measure the velocity field in cross-flow planes passing through the trailing vortical structures, with image magnification and location guided by the dye injection results. Reynolds numbers of 8000–24,000 were partially chosen as a compromise between dye injection quality, facility size, and model blockage in the test section. All models were chosen to have an aspect ratio of 2.0. Planform geometries consisted of a rectangle, a semi-ellipse, and delta wing. Delta wings are rarely found in use for practical MAVs; however, a delta wing is a natural choice for attempting to produce usable lift over the broad range of angle of attack expected to be encountered by MAVs.

This study focuses on the connection between the coefficients of lift, experimentally obtained from studying trailing vortex structure (and circulation) at low Reynolds numbers (8000–24,000), experimentally obtained through force measurement, and inviscid theoretically obtained predictions. Trailing vortex roll-up and formation is also observed with the help of flow visualization. Lift is calculated from the Kutta–Joukowski theorem, $L = \rho_\infty V_\infty \Gamma b'$, using peak circulation from area integrations of the vorticity field in the cross-flow plane as measured with digital particle image velocimetry. b' is taken as the effective span: namely, twice the distance between the observable core of the trailing vortex and the wing centerplane.

Experiments were conducted in the Air Force Research Lab, Air Vehicles Directorate's horizontal free-surface water tunnel (HFWT). The test section is 1.5 ft wide, 2 ft high, and 9 ft long. The contraction ratio is 4:1, with two honeycomb screens and three wire-mesh screens. A 12 in. axial impeller driven by a 15 hp motor gives a flow velocity range of about 1.5 to 18 in./s. Single-component hot-film measurements give a streamwise turbulence intensity of $\sim$0.1% at speeds between 3 and 15 in/s. The particles used for DPIV were TiO_2, with mean diameter of 2–3 microns. Images were taken with a 30 Hz UniqVision UP-1830 1000 $\times$ 1000 $\times$ 8-bit Progressive Scan CCD Camera, using a 20 mm Nikon F-mount lens for flow visualization, and 60 mm macrolens for DPIV. The laser was a New Wave Research Solo DPIV, double-pulsed 125 mJ/pulse, 15 pulse/s Nd:YAg, with beam-forming optics consisting of two spherical and two cylindrical lenses, as suggested by Raffel et al. [20]. Conventions for the coordinate system are given in Fig. 1. The uncertainty in the measurements of the velocity vectors and the calculation of the coefficient of lift is within 5%, which results from averaging only 90 sets of individual velocity vector fields for each test in Table 2. The inaccuracy in the calculation of vortex position relative to the wing tip is on the order of 2 pixels, resulting in an uncertainty of $\sim$2% based on $\bar{c}$.

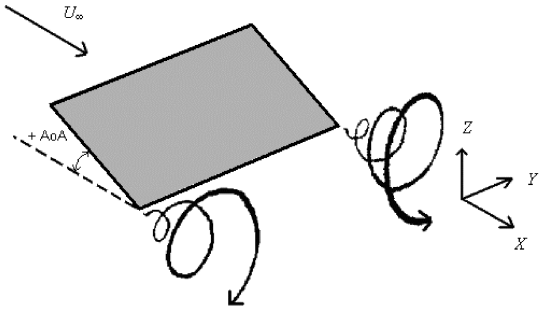

Fig. 1 Coordinate system definition.

Flow visualization by dye injection was used for qualitative observation of the formation of the vortex system, evolution of the vortex system over different positions downstream of the trailing edge, and to estimate the maximum velocity in the axial (streamwise) direction. The latter was used to help select PIV light sheet thickness and streamwise offset in the light sheet pair, to improve PIV cross-correlations.

Flat-plate models were manufactured from 1.5 mm-thick 300 series stainless steel and painted flat black to minimize laser reflection. The model parameters and dimensions were chosen such that the aspect ratio and planform area for all three wings were identical. The only variation was the planform geometry (see Fig. 2). The common mean aerodynamic chord is $\bar{c} = 10$ cm, the span is 20 cm, the aspect ratio is 2, the planform area is 0.02 m^2, and the thickness to chord ratio is 0.0075 for all three models.

For the rectangular and semi-elliptical wings, the dye injection tube was placed near the wing tip. For the delta wing, the dye tube was placed as is usually done for delta wings, near the apex of the wing, in the vicinity of the windward-side stagnation point. The flow visualization test matrix is given in Table 1. The angle of attack range was selected to be from low angle of attack to before or near-stall at the lowest Reynolds number tested. The DPIV test matrix is given in Table 2. The choices for downstream interrogation planes were selected specifically to remain in the near wake. Potentially large differences in separation bubble behavior were expected across the Reynolds number range selected.

The force balance used was a Rolling Hills Research Corporation (RHRC) five-component internal strain-gauge balance. The RHRC balance is designed to measure normal force, side force, pitching moment, yaw moment, and rolling moment. It is composed of 1000-Ohm semiconductor gauges with a gauge factor of 145 and a resolution of 1% of maximum calibrated load.

The individual gauge channel sensitivities are as follows:

Normal force: 2.07 V/lb

Side force: 11.94 V/lb

Pitching moment: 2.76 V/in. · lb

Table 1 Flow visualization test matrix

	$U_\infty = 9$ cm/s ($Re = 8028$)			
	Angle of attack, deg			
Semi-ellipse	5	10	——	——
Rectangle	5	10	15	20
Delta	——	10	15	——

Yaw moment: 7.90 V/in. · lb

Rolling moment: 1.19 V/in. · lb

Data were acquired using a National Instruments 6053E data acquisition card. For each individual data point presented, sampling was performed at 100 Hz for 15 s, and then averaged across three independent runs for a total of 4500 samples. As there is no axial stage on the RHRC balance, the balance's measurement of "lift" is really normal force. The measured normal force was multiplied by $\cos(\alpha)$ to more appropriately compare with lift.

Results

Flow Visualization

The most prominent difference in the flow around the models is in the symmetry and structure of the trailing vortex. The rectangular wing produced the most coherent and most spatially periodic vortex roll-up. As shown in Fig. 3, the vortex sheds from the wing tip downstream of the trailing edge with an azimuthal velocity of approximately 1/3 of the freestream velocity, as determined based on known camera frame rate (30 fps) and the interframe progression of dye upon opening the dye valve. The vortex helical geometry stabilizes at about $X/C = 0.5$ downstream of the trailing edge, whereupon the vertical-plane component of the dye streak appears to acquire a slight upwash.

Figure 4 shows the classical primary leading-edge vortices emanating from the apex of the wing, with a nearly straight-line trajectory of about 16 deg sweep. There is a gradual onset of helical motion in the dye streak around the trailing-edge location, but unlike for the rectangular wing, a markedly periodic helix was not found. Visualization of tip vortices was unsuccessful, and interaction between leading- and trailing-edge vortices could not be identified through dye injection. However, the delta wing, unlike the rectangular wing, has a wake vortex trajectory consistent with the downwash direction. Some dye is also entrained in the wake of the dye probe.

The semi-elliptical wing in Fig. 5 is an intermediate case, with successfully visualized but highly incoherent tip vortices, conceivably due to interaction between leading-edge vortices and tip vortices but without a geometrically-fixed point of leading-edge vortex origin. The elliptical leading edge creates not only multiple secondary vortices, but also very significant spanwise flow, as

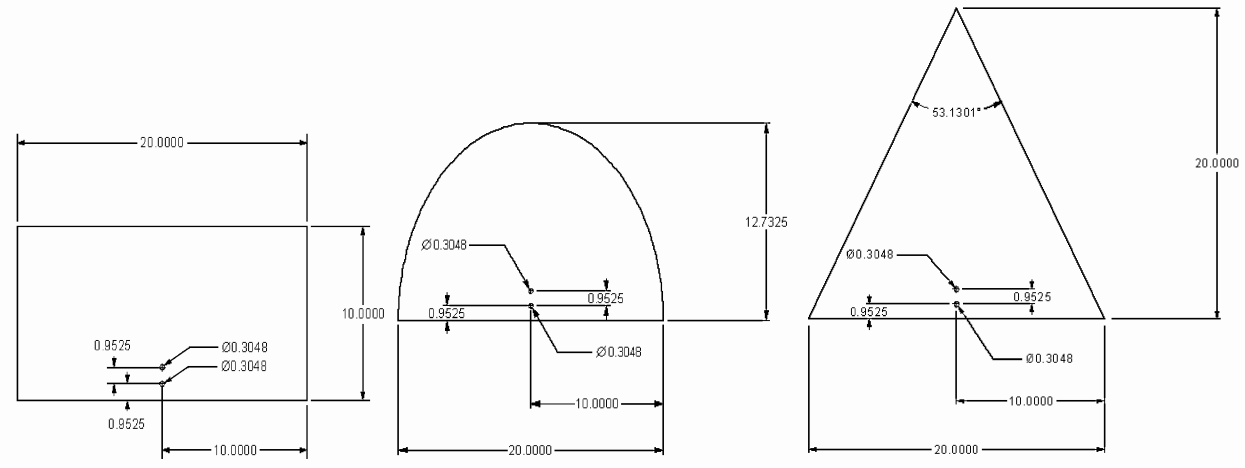

Fig. 2 The three models, each of AR = 2: rectangular, delta, and semi-ellipse (dimensions in centimeters).

Table 2 DPIV test matrix

	$U_\infty = 0.09$ m/s ($Re = 8028$)			$U_\infty = 0.27$ m/s ($Re = 24,083$)		
	$X/C = 0.1$	$X/C = 1$	$X/C = 2$	$X/C = 0.1$	$X/C = 1$	$X/C = 2$
	AoA, deg	AoA, deg	AoA, deg	AoA, deg	AoA, deg	AoA, deg
Semi-ellipse	10	10	10	10	10	10
	15	15	——	15	15	——
Rectangle	5	5	5	5	5	5
	10	10	10	10	10	10
	15	15	——	15	15	——
Delta	10	10	——	10	10	——
	15	15	——	15	15	——

determined based on the angle of the spanwise deflection of the dye when the tube was moved to the root of the model; at the root of the semi-ellipse, dye is deflected spanwise at nearly 45 deg. For the rectangular wing, on the other hand, the observed spanwise flow velocity component was less than 10% of the streamwise component.

DPIV Measurements

Flow visualization implied that the rectangular wing had the most coherent trailing vortex structure, followed by the delta and lastly by the semi-ellipse. When averaging a sequence of DPIV image pairs, it is expected that smearing and attenuation of velocity peaks would follow a similar progression. Representative contour plots of averaged velocity in cross-flow planes and the associated component of vorticity are given in Figs. 6–8, covering two different Reynolds numbers and two different angles of attack. The velocity is magnitude of in-plane velocity, normalized by freestream U_∞. The vorticity is the single (out-of-plane) component, normalized by $\bar{c}/U_\infty$. The projection of the trailing edge of the wing is in each case marked with a black line segment; the segment shown represents the wing semispan. Because of the large parameter space and the limitations of the data storage system (images were written directly to

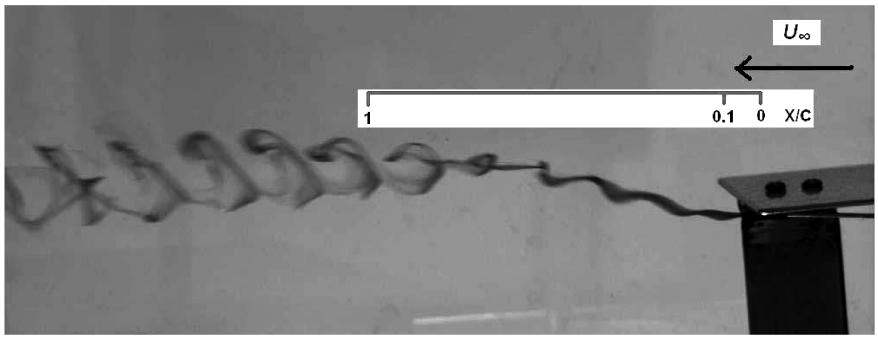

Fig. 3 Rectangular wing: 5 deg AoA, $Re = 8028$, flow visualization.

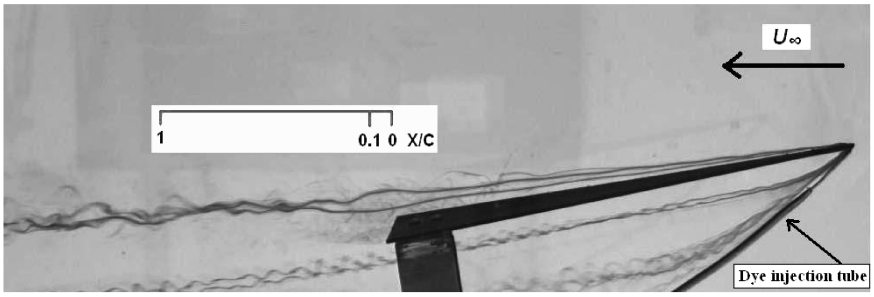

Fig. 4 Delta wing: 10 deg AoA, $Re = 8028$, flow visualization.

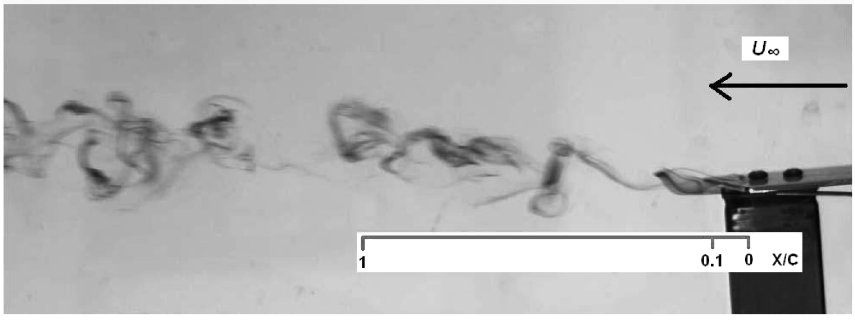

Fig. 5 Semi-elliptical wing: 5 deg AoA, $Re = 8028$, flow visualization.

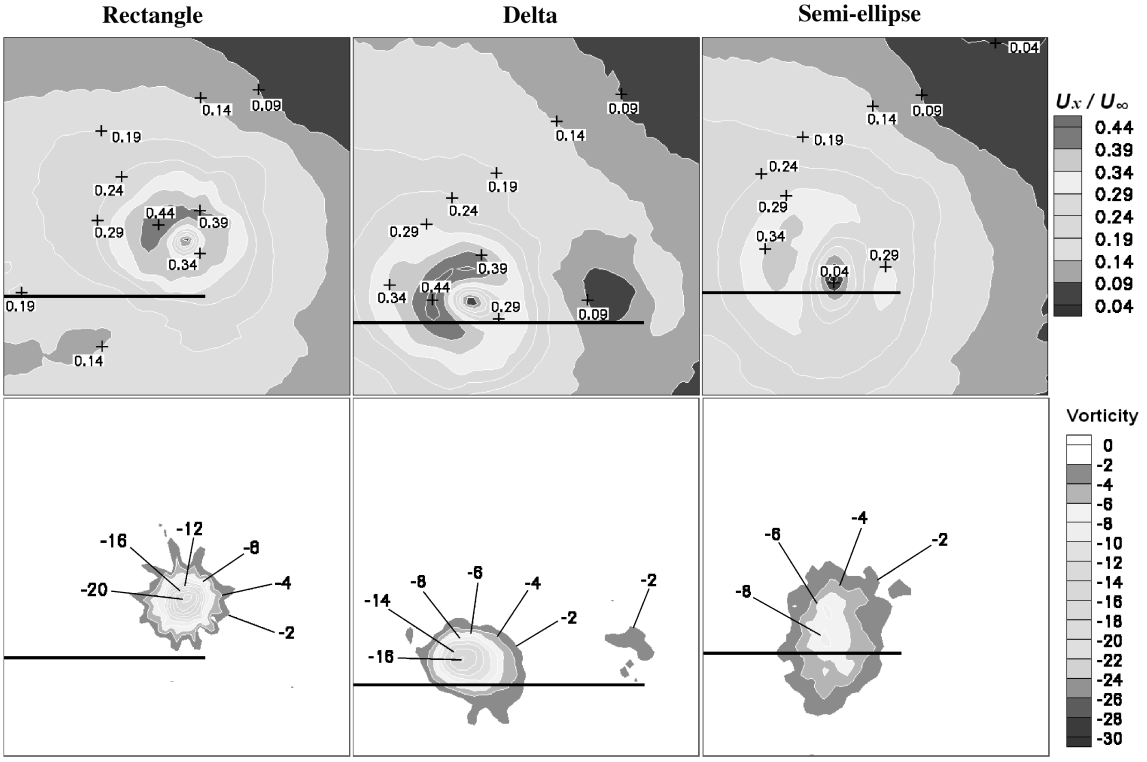

Fig. 6 In-plane velocity magnitude and out-of-plane vorticity: $\alpha = 10$ deg, downstream $X/C = 1$, $U_\infty = 9$ cm/s, $Re = 8028$.

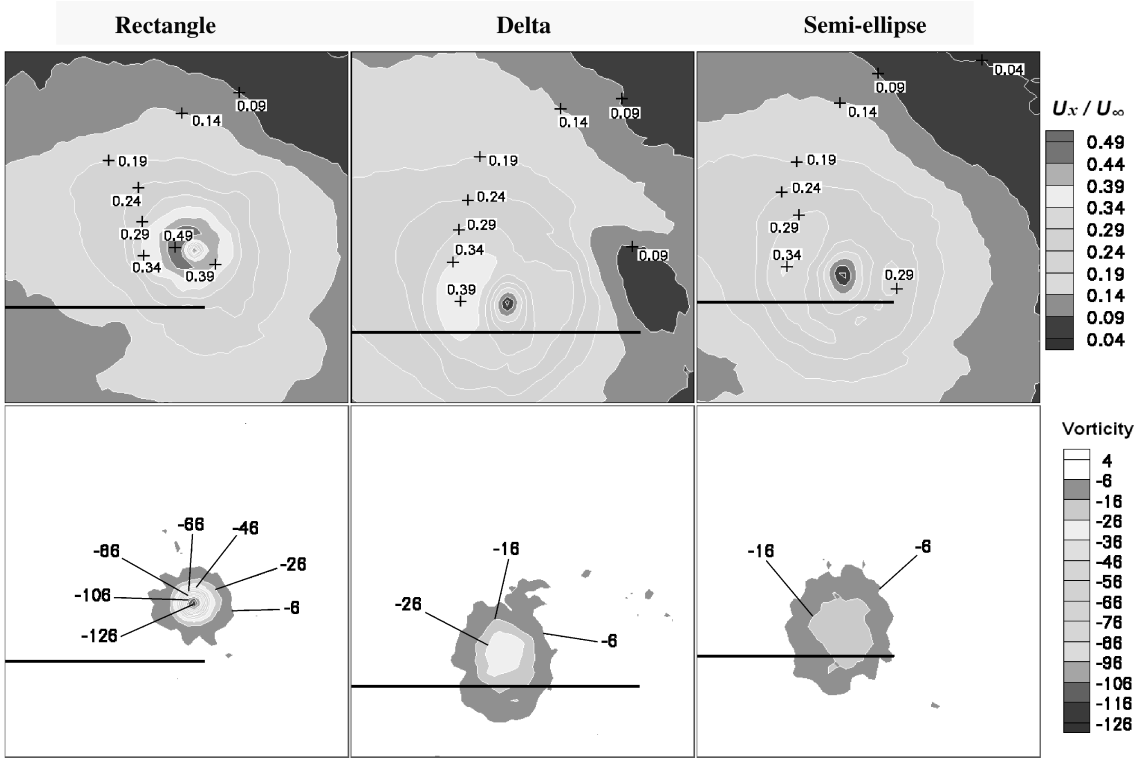

Fig. 7 In-plane velocity and out-of-plane vorticity: $\alpha = 10$ deg, downstream $X/C = 1$, $U_\infty = 27$ cm/s, $Re = 24,083$.

computer RAM), only 90 DPIV pairs were used for assembling the flow statistics. It is noted that although peak locking can be observed in many of the processed images, only integrated quantities (circulation) were derived from these images and used in the results.

Velocimetry results showed that the rectangular wing in all cases indeed had the tightest vortical structure, the highest vorticity magnitude, and the largest azimuthal velocity; at $\alpha = 15$ deg it is on the order of $0.6U_\infty$, compared to the delta's $0.5U_\infty$ and the semi-ellipse's $0.4U_\infty$, at both $Re = 8028$ and $Re = 24,083$. The next largest vorticity is present in the delta-wing wake, where primary leading-edge vortices are dominant. The wing-tip vortices for the semi-elliptical wing are the least stable out of the three models leading to the smallest averaged azimuthal velocity. This is most likely due to the complex leading edge of the semi-elliptical planform. Single-pair DPIV images also show that the semi-elliptical wing produced the most secondary vortices.

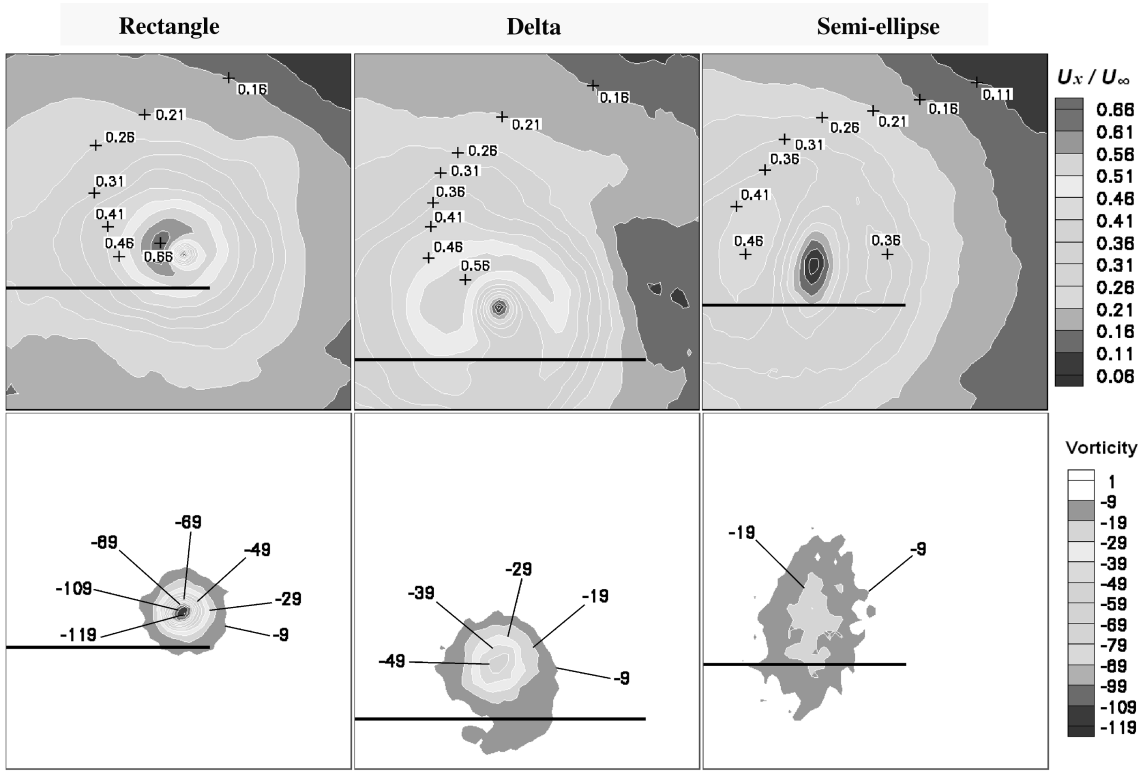

Fig. 8 In-plane velocity and out-of-plane vorticity: $\alpha = 15$ deg, downstream $X/C = 1$, $U_\infty = 27$ cm/s, $Re = 24,083$.

Circulation was calculated by integrating in each cross-flow plane the vorticity values over the area interior to circular contours of progressively increasing radii, centered about the coordinates of vorticity maxima. For purposes of calculating lift from circulation according to $L = \rho_\infty V_\infty \Gamma b'$, the peak value of circulation was taken for each respective case. Curves of circulation, normalized by freestream velocity and wing geometric span, are plotted vs radius of circular contour, again normalized by geometric wing, in Fig. 9. Because the circulation was calculated using the ensemble-averaged velocity data, fluctuations such as wandering of the vortex trajectory could be responsible for attenuation of circulation peak values; this effect was not investigated. The change in concavity of the circulation curves at radii above that of the peak circulation value is due to the potentially significant contribution of the opposite sense of rotation of branching vortices.

For the rectangle and the semi-ellipse, at $Re = 8000$ the circulation peak is slightly (by up to about 15%) higher than for $Re = 24,000$, at every streamwise location, at $\alpha = 5$ and 10 deg. At $\alpha = 15$ deg, approaching stall, there is little Reynolds number dependency. For the $\alpha = 10$ deg case, for which the largest amount of data were available, it is evident that the semi-ellipse persistently exhibits about 10–20% higher peak circulation than the rectangle: at every respective streamwise location and both Reynolds numbers. For the 5 deg case, for which only rectangle-wing measurements

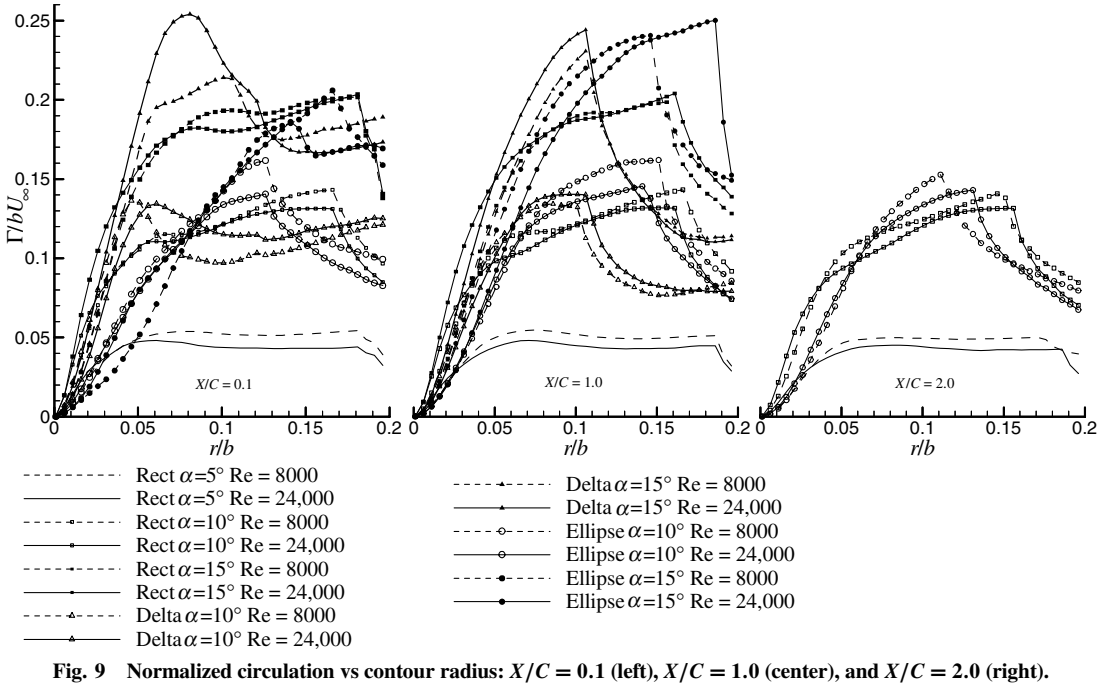

Fig. 9 Normalized circulation vs contour radius: $X/C = 0.1$ (left), $X/C = 1.0$ (center), and $X/C = 2.0$ (right).

were available, the lack of streamwise variation in the circulation curves is especially noticeable. This is largely also true at 10 deg, again for both the rectangle and semi-ellipse. Such lack of streamwise variation suggests that the vortex wake is largely rolled-up even at $X/C = 0.10$, at least for like-signed vortical structures coherently adding to form the net circulation, and at angles of attack well below stall. Lack of streamwise variation in peak circuluation is of course consistent with Kelvin's theorem, supporting the assertion that dissipative effects are negligible and that the production of vorticity due to the wing is fully accounted for in the cross-flow plane integration. For $\alpha = 15$ deg the rectangle still remains largely streamwise-invariant, but the semi-ellipse has a noticeable increase in peak circulation in going from $X/C = 0.1$ to $X/C = 1.0$.

Though the ellipse has a less coherent wake, as judged from vorticity contour plots and flow visualization, it tends to attain maximum circulation over a contour of smaller radius than does the rectangle. The delta wing attains its peak circulation of the smallest-radius contour. At $X/C = 0.1$, the delta wing has the distinctive behavior of a smooth decrease in circulation after attaining its maximum, whereas in every other case, the post-peak dropoff has a discontinuity in slope. Also at $X/C = 0.1$, the delta wing had the largest difference between $Re = 8000$ and $Re = 24,000$ behavior. Conceivably these phenomena could be attributed to interaction of the leading-edge and tip vortices, which would be expected to be prominent at $X/C = 0.1$.

The streamwise evolution of vorticity (that is, of the streamwise-direction component of vorticity) is shown in Figs. 10–12 for the rectangle, delta, and semi-ellipse, respectively, for the $Re \sim 8000$ and $Re \sim 24,000$ cases. The rectangle achieves much higher values of peak vorticity relative to the other two wings; the ellipse achieves the least, but also has the most diffuse wake, consistent with the observation of comparable peak circulation. Qualitatively there was no appreciable change in vorticity contour shape between $Re = 8000$ and $Re = 24,000$ for any of the wings. For the delta wing, the characteristic leading-edge primary vortex and feeding sheet are clearly visible at $X/C = 0.1$, with what appears to be a secondary vortex with vorticity of opposite sign, closer to the plane of the trailing edge. By $X/C = 1.0$ the feeding sheet and secondary vortex are gone, leaving behind a single vortical structure indistinguishable from a tip vortex. For all wings, but especially for the rectangle, vorticity attributable to the suction-side wing boundary layer is visible at $X/C = 0.1$ as a thin sheet immediately above the plane of the trailing edge.

The calculation of lift coefficient, as shown in Figs. 13–15 (again for the rectangle, delta, and semi-ellipse, respectively), is largely independent of the streamwise location at which peak circulation was evaluated. This was the case for all of the wings and both of the Reynolds numbers tested. Streamwise variation of lift coefficient is attributable to either an apparent change in circulation, or change in the vortex spacing (that is, the effective span). Because the former should remain constant by Kelvin's theorem, streamwise variation in calculated lift would be attributable to evolution of the vortex spacing.

Velocimetry results were also used to compare direction of the dominant vortical structures with the inferences available from flow visualization. Downstream evolution of vortex position in cross-flow planes, relative to the wing tip, is shown in Figs. 16–18, for the rectangle, delta, and ellipse, respectively. The wing tip location is at $Y/b = 0.5$ and $Z/C = 0$; the root of the wing at the trailing edge is at $Y/b = 0$ and $Z/C = 0$. The arrows denote the downstream direction; that is, going from $X/C = 0.1$ to 1.0 and 2.0.

For all cases, at $X/C = 0.1$ the vortex trajectory commences inboard and above the wing tip, with gradual downwash in going to $X/C = 1$ and $X/C = 2$. At these Reynolds numbers, each wing is

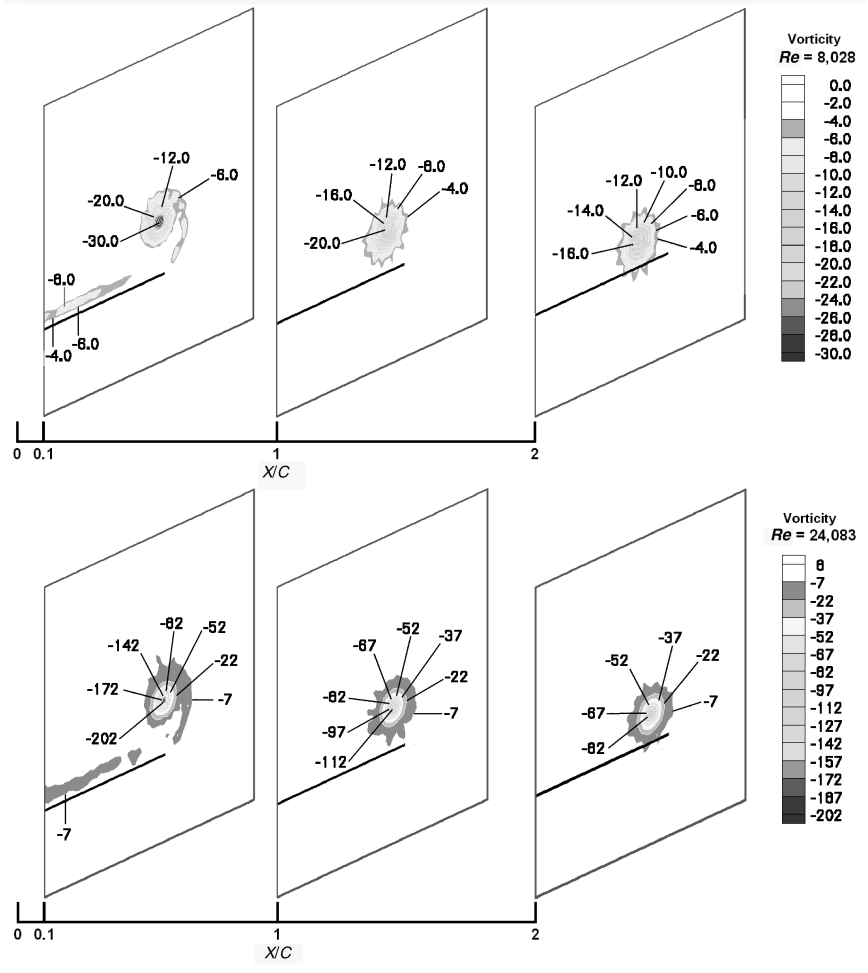

Fig. 10 Vorticity evolution vs distance downstream from trailing edge; rectangle at $\alpha = 10$ deg.

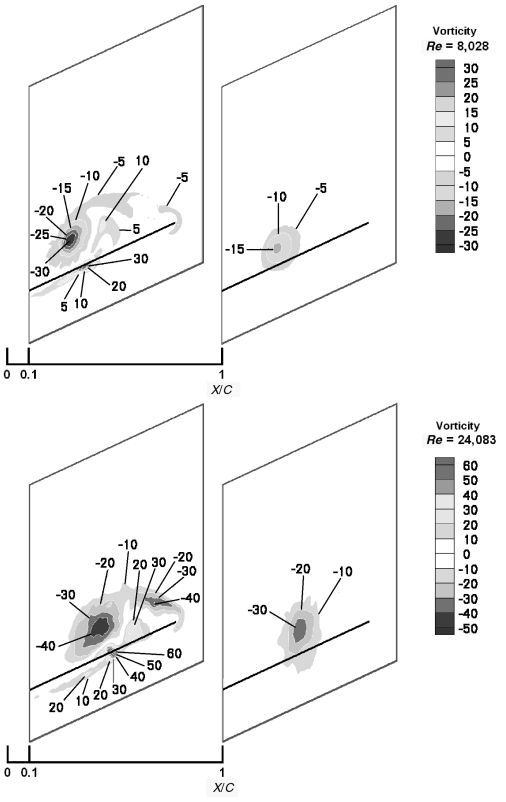

Fig. 11 Vorticity evolution vs distance downstream from trailing edge; delta at $\alpha = 10$ deg.

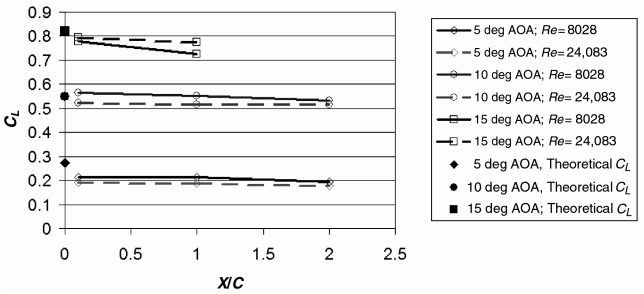

Fig. 13 C_L vs X/C comparison for rectangle.

believed to act in some sense as a bluff body, with a low-pressure wake behind and above the trailing edge at positive angle of attack. The region of low pressure entrains the tip vortices, whereas in the global sense a downwash consistent with net positive lift is present. Thus, the vortex system is offset upwards by the viscous wake. This better explains the flow visualization results, where dye injected at the wing tip is slowly entrained into the viscous wake, eventually tracking the tip vortex core. At $X/C = 0.1$, for example, the dye streak is not coincident with the tip vortex core trajectory. Curiously, in some cases the vertical offset of the trailing vortex system is generally higher for the $Re \sim 24,000$ case than for the $Re \sim 8000$ case.

For the rectangle in all cases and for the semi-ellipse except at $Re \sim 24,000$ and $\alpha = 10$ deg, the vortices moved inboard in going downstream. For the delta wing the vortex trajectory was persistently outboard: suggesting that with PIV, as with dye injection, the mixing process between the tip vortices and leading-edge vortices was not fully resolved.

Lift Coefficient Comparison

Predictions for lift coefficient from slender-wing and lifting-surface (with suction analogy) theories are compared with force balance and PIV results in Figs. 19–22. For AR = 2, the two theoretical predictions are very similar, as the lifting-surface theory's nonlinearity is very slight. Also, the two predictions are identical across the three planforms, because K_P and K_V are taken to be the same regardless of planform [19]. The theoretical predictions are not intended to account for stall. In particular, failure of the leading-edge or side-edge vortex sheet to reattach towards the wing suction-side would of course call into question the suction-analogy assumptions.

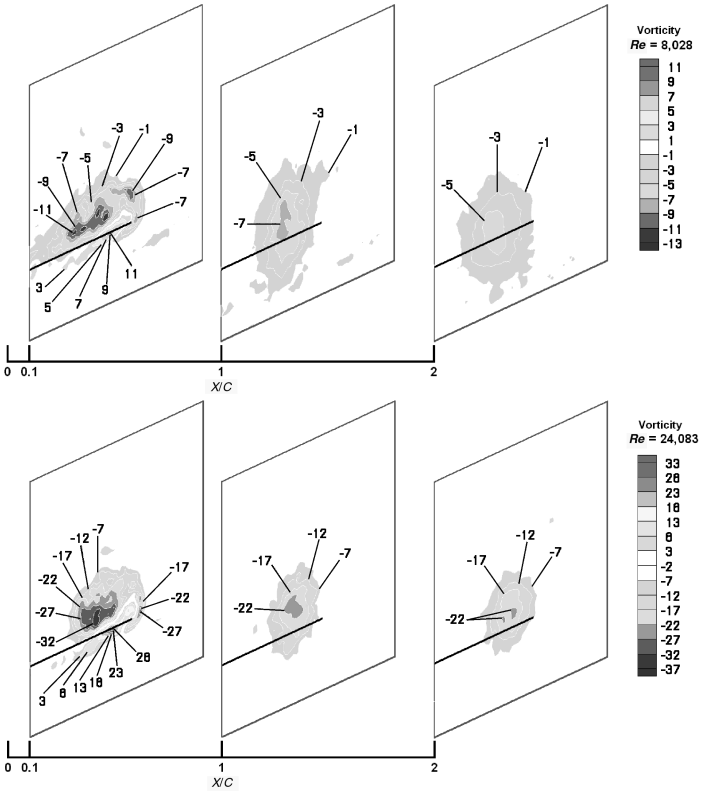

Fig. 12 Vorticity evolution vs distance downstream from trailing edge; semi-ellipse at $\alpha = 10$ deg.

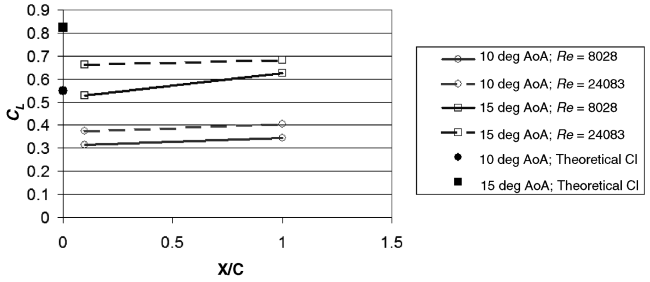

Fig. 14 C_L vs X/C comparison for delta wing.

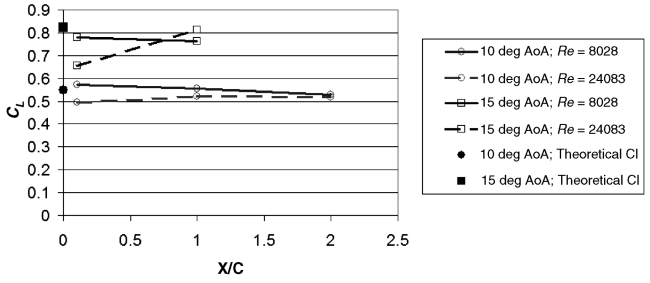

Fig. 15 C_L vs X/C comparison for semi-ellipse.

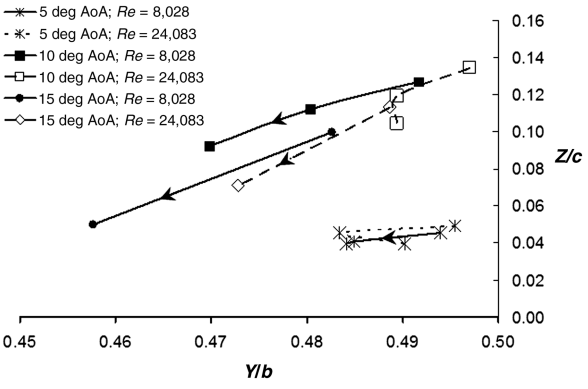

Fig. 16 Downstream evolution of vortex center location: rectangle.

The rectangular wing force balance data (Fig. 19) follow the theory through $\alpha = 15$ deg. Uncertainty/error bars were placed in the figure for the experimental data; however, the degree of uncertainty falls into the range of the size of the symbols for the data points. The main disagreement with the theoretical predictions is a maximum relative difference on the order of 27% for the rectangle at $\alpha = 5$ deg, where the absolute difference in coefficient of lift as calculated from circulation is $\sim$0.074. The force balance results are compared with those of Laitone [13] for Re $\sim 20,000$ (Fig. 20); the present results for AR $= 2$ were rescaled to AR $= 2.18$ by the ratio of

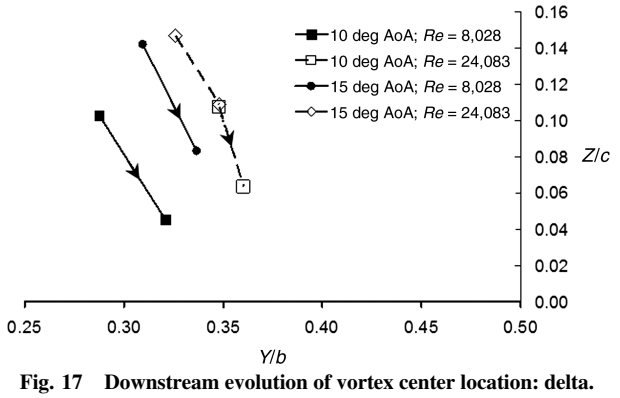

Fig. 17 Downstream evolution of vortex center location: delta.

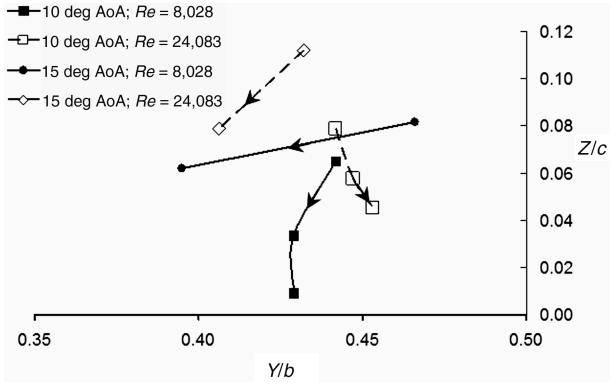

Fig. 18 Downstream evolution of vortex center location: semi-ellipse.

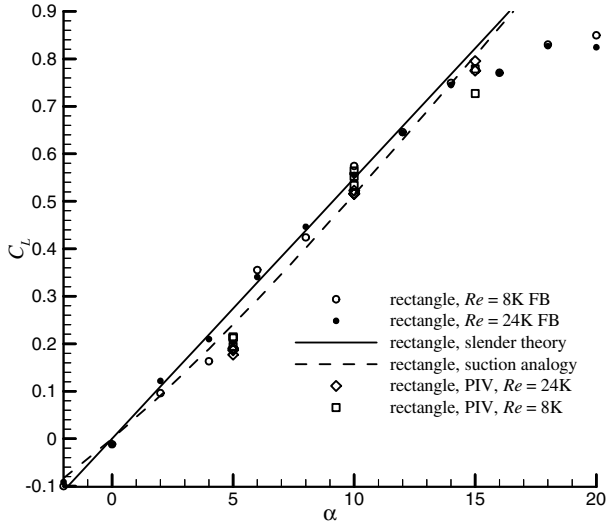

Fig. 19 C_L vs α: AR $= 2$ rectangle.

aspect ratios, to compare with Laitone's experiment. After such rescaling, the force balance results are essentially coincident up to onset of stall, at around $\alpha = 13$ deg. PIV-based results for the rectangle-wing lift (Fig. 19) show scatter due to downstream location at which circulation is computed that exceeds data spread due to Reynolds number effects. This scatter is due mostly to the reduction in spanwise separation between the port and starboard tip vortices, and thus a reduction in effective span. However, the PIV-based results essentially bracket the force balance-derived lift curve. This suggests a very modest (if any) Reynolds number dependency of the PIV measurements, and general viability of the technique.

Delta wing force balance results (Fig. 21) likewise show good agreement with theoretical prediction. A slight nonlinearity in the force balance data tends to follow the suction-analogy curve at angles of attack through 20 deg, suggesting that the delta planform is especially well suited to the suction analogy. Not surprisingly, the highest uncertainty in force balance data occurs at the lowest angles of attack, where loads are lowest, and again at the highest angles of attack, where the absence of expected axial stage contributions to lift force becomes more apparent. From the force data, onset of stall (or perhaps more properly, integrated effects of breakdown of a coherent leading-edge vortical system) commences near $\alpha = 25$ deg. For the higher Reynolds number, the stall process is gentler. The PIV-derived lift coefficients for the delta wing show an interesting trend: based on vortex span, the data significantly underpredict the force balance result, and show large variation depending on streamwise sampling location. But if instead lift is calculated based on geometric span, scatter is much reduced, and the data converge towards the force balance results, implying that geometric span is evidently the more relevant length scale. Of the three configurations, the delta wing stalls at the highest angle of attack, thus attaining the highest

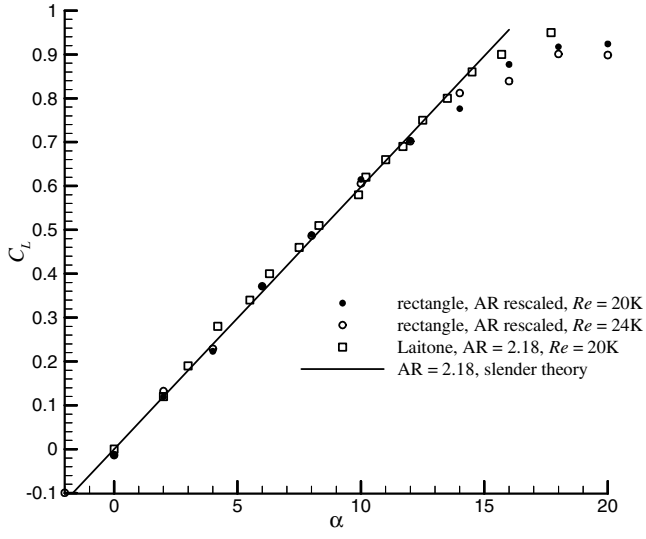

Fig. 20 C_L vs α for rectangles; comparison with Laitone [13].

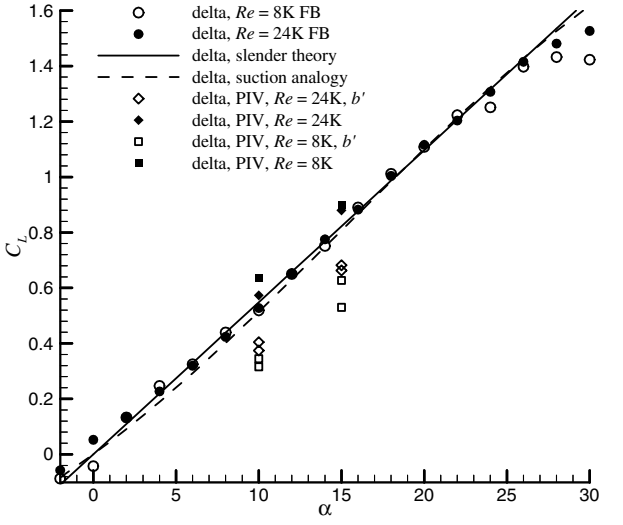

Fig. 21 C_L vs α: AR = 2 delta wing.

maximum lift coefficient. However, below the onset of stall, the lift curves of the three configurations are quite alike: a result consistent with theoretical inviscid predictions.

Force balance data for the semi-ellipse (Fig. 22) closely follow the suction-analogy predictions up through the onset of stall, at around $\alpha = 14$ deg. As with the delta wing, the $Re = 8000$ and $Re = 24,000$ force balance data are essentially indistinguishable below stall angles of attack. PIV-based lift data, again using vortex span, compare well with the force balance data at $\alpha = 10$ deg, and somewhat underpredict at $\alpha = 10$ deg. The $Re = 24,000$ case shows dependency on streamwise location, due to the reduction in vortex span as the trailing vortex system evolves. Recalling Fig. 9 at $X/C = 1.0$, the semi-ellipse has the highest circulation peak of the three wings. Thus, to some extent as in the case of the delta wing, use of vortex span as opposed to geometric span can result in underprediction of lift coefficient.

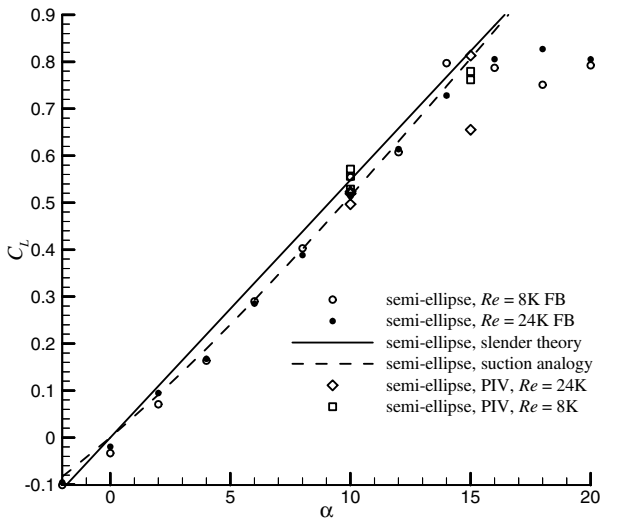

Fig. 22 C_L vs α: AR = 2 semi-ellipse.

Conclusions

For thin, flat plates of AR = 2 and three planform shapes (rectangle, delta wing, and semi-ellipse) at $Re = 8000$ and $Re = 24,000$, viscous effects do not detract from the validity of classical slender- and swept-wing theories in predicting lift coefficient up to stall. Application of the Kutta–Joukowski theorem, when modified to be based on vortex span, is moderately successful in arriving at the correct value of lift coefficient based on circulation, as calculated from particle image velocimetry in cross-flow planes in the near wake. For all three wings, the lift curve slope ($\sim\pi$) does not depend on planform shape or on Reynolds number, despite the differences in wake structure, as elucidated by DPIV and dye injection. Whereas the rectangular wing had the tightest roll-up of vorticity into tip vortices, and the highest magnitudes of vorticity peaks, the integrated maximum circulation was not appreciably different from the other wings. For the delta wing, tip vortices were not readily discernable, and thus an interaction between leading-edge vortices and tip vortices was not observed. The semi-ellipse had the least coherent vortical structure, evidently due to the lack of either a well-defined apex or a large-chord wing tip.

The stability of the vortex center location for all angles of attack at $Re = 8000$ and $Re = 24,000$, would also appear to be related to planform geometry complexity. The location of the vortex center is least stable for delta and semi-elliptical wings at the lowest Reynolds numbers tested. The vortex center seems to fluctuate to produce dual-core vortices in some cases, which are not present in the individual image pairs, suggesting unstable primary vortex position.

The main impact of viscosity was on an apparent upwash of the trailing vortex system in the near wake, evidently due to a bluff-body-like wake with a low-pressure region that entrained the injected dye. Thus, this is yet another example where care needs to be taken when interpreting dye streak evolution as indicative of the vortex core.

Avenues for further study include DPIV measurements of wake momentum deficit or direct force measurement of drag to compare lift to drag ratio for the various models, cambered plates vs flat plates, and extension of measurements to yet lower Reynolds numbers.

References

[1] Mueller, T. J., "An Overview of Micro Air Vehicle Aerodynamics," *Fixed and Flapping Wing Aerodynamics for Micro Air Vehicle Applications*, edited by T. J. Mueller, Progress in Aeronautics and Astronautics, Vol. 195, AIAA, Reston, VA, 2001, pp. 1–9.

[2] Grasmeyer, J. M., and Keennon, M., "Development of the Black Widow Micro Air Vehicle," AIAA Paper 2001-0127, 2001.

[3] Ifju, P., Stanford, B., Sytsma, M., and Albertani, R., "Analysis of a Flexible Wing Micro Air Vehicle," AIAA Paper 2006-3311, 2006.

[4] Viieru, D., Tang, J., Lian, Y., Liu, H., and Shyy, W., "Flapping and Flexible Wing Aerodynamics of Low Reynolds Number Flight Vehicles," AIAA Paper 2006-0503, 2006.

[5] Ol, M., McAuliffe, B. R., Hanff, E. S., Scholz, U., and Kaehler, C., "Comparison of Laminar Separation Bubble Measurements on a Low Reynolds Number Airfoil in Three Facilities," AIAA Paper 2005-5149, 2005.

[6] Yuan, W., Khalid, M., Windte, J., Scholz, U., and Radespiel, R., "An Investigation of Low-Reynolds-Number Flows Past Airfoils," AIAA Paper 2005-4607, 2005.

[7] Gad-el-Hak, M., "Micro-Air-Vehicles: Can They be Controlled Better?," *Journal of Aircraft*, Vol. 38, No. 3, May–June 2001, pp. 419–

429.
[8] Gursul, I., Taylor, G., and Wooding, C. L., "Vortex Flows over Fixed-Wing Micro Air Vehicles," AIAA Paper 2002-0698, 2002.
[9] Spedding, G., McArthur, J. M., and Rosen, M., "Deducing Aerodynamic Mechanisms from Near- and Far-Wake Measurements of Fixed and Flapping Wings at Moderate Reynolds Number," AIAA Paper 2006-33, 2006.
[10] Torres, G. E., and Mueller, T. J., "Aerodynamic Characteristics of Low Aspect Ratio Wings at Low Reynolds Numbers," *Fixed And Flapping Wing Aerodynamics For Micro Air Vehicles Applications*, edited by T. J. Mueller, Progress in Aeronautics and Astronautics, Vol. 195, AIAA, Reston, VA, 2001, Chap. 7, pp. 115–139.
[11] Mueller, T. J., "Low Reynolds Number Vehicles," AGARDograph AG-288, 1985.
[12] Polhamus, E. C., "Predictions of Vortex-Lift Characteristics by a Leading-Edge-Suction Analogy," *Journal of Aircraft*, Vol. 8, No. 4, 1971, pp. 193–199.
[13] Laitone, E. V., "Wind Tunnel Tests of Wings at Reynolds Numbers Below 70,000," *Experiments in Fluids*, Vol. 23, No. 5, 1997, pp. 405–409.
[14] Lowson, M. V., "Visualization Measurements of Vortex Flows," AIAA Paper 1989-0191, 1990.
[15] Cosyn, P., and Vierendeels, J., "Numerical Investigation of Low Aspect Ratio Wings at Low Reynolds Numbers," AIAA Paper 2005-4609, 2005.
[16] Zuhal, L., and Gharib, M., "Near Field Dynamics of Wing Tip Vortices," AIAA Paper 2001-2710, 2001.
[17] Thwaites, B., *Incompressible Aerodynamics: An Account of the Theory and Observation of the Steady Flow of Incompressible Fluid Past Aerofoils, Wings, and Other Bodies*, Dover, New York, 1960, p. 314.
[18] Anderson, J. D., Jr., *Fundamentals of Aerodynamics*, 2nd ed., McGraw–Hill, New York, 1991, p. 343.
[19] Lamar, J. E., "Extension of Leading-Edge-Suction Analogy to Wings with Separated Flow Around the Side Edges at Subsonic Speeds," NASA TR R-428, 1974.
[20] Raffel, M., Willert, C. E., and Kompenhans, J., *Particle Image Velocimetry—A Practical Guide*, Springer, Berlin, 1998.